Supporting information

Revisiting of $Na_{2/3}Ni_{1/3}Mn_{2/3}O_2$ Cathode: Oxygen Redox Chemistry and Oxygen Release Suppressing

Yi Zhang,[1] Miaomiao Wu,[1] Jiwei Ma,[1] Guangfeng Wei,[2] Yun Ling,[3] Renyuan Zhang*[1] and Yunhui Huang*[1]

Experimental Section

Synthesis of Na$_{2/3}$Ni$_{1/3}$Mn$_{2/3}$O$_2$

Na$_{2/3}$Ni$_{1/3}$Mn$_{2/3}$O$_2$ compound was prepared by sol-gel method. Stoichiometric NaAc, Fe(NO$_3$)$_3$, NiAc$_2$ and MnAc$_2$ (Ac = CH$_3$COO$^-$) were dissolved in 40 mL deionized water to form a dark red solution. 5% excess NaAc was added to compensate the sodium loss at high temperature. The solution was totally evaporated at 80 °C to achieve powder precurser. The precurser was first sintered in O$_2$ atmosphere at 350 °C for 4 h and then at 900 °C for another 12 h with a heating rate of 2 °C min^{-1}. The obtained sample was quenched to room temperature and then transfered to drying room.

Synthesis of Na$_{2/3}$Mn$_{5/6}$O$_2$

Na$_{2/3}$Mn$_{5/6}$O$_2$ compound was prepared by sol-gel method. Stoichiometric NaAc, and MnO$_2$ (Ac = CH$_3$COO$^-$) were mixed togather. The precurser was first sintered in O$_2$ atmosphere at 350 °C for 4 h and then at 600 °C for another 12 h with a heating rate of 2 °C min^{-1}. The obtained samples was quenched to room temperature and then transfered to drying room.

Synthesis of Na$_{2/3}$Fe$_{2/9}$Ni$_{2/9}$Mn$_{5/9}$O$_2$

Na$_{2/3}$Fe$_{2/9}$Ni$_{2/9}$Mn$_{5/9}$O$_2$ compound was prepared by sol-gel method. Stoichiometric NaAc, Fe(NO$_3$)$_3$, NiAc$_2$ and MnAc$_2$ (Ac = CH$_3$COO$^-$) were dissolved in 40 mL deionized water to form a dark red solution. 5% excess NaAc was added to compensate the sodium loss at high temperature. The solution was totally evaporated at 80 °C to achieve powder precurser. The precurser was first sintered in O$_2$ atmosphere at 350 °C for 4 h and then at 900 °C for another 12 h with a heating rate of 2 °C min^{-1}. The obtained sample was quenched to room temperature and then transfered to drying room.

Electrochemical Measurements for SIB

The electrochemical test were carried out using CR2032 coin-type cells with the obtained samples as cathode, sodium disc as anode and glass fiber (whatman GF/D) as separator. For preparation of cathode electrodes, a homogeneous slurry was first obtained by mixing 80 wt% active material, 10 wt% Ketjen black (EC600JD) and 10 wt% poly(vinyl difluoride) (PVDF) in N-methylpyrrolidinone (NMP), and then the slurry was pasted uniformly onto aluminum foil current collector and dried in vacuum at 95 °C for 12 h. The loading mass of the active material was 2-2.5 mg cm^{-2}. The electrolyte was a mixture solution of ethylene carbonate and dimethyl carbonate 1:1 (w/w) containing 1 M NaClO$_4$ and 5 wt% flouroethylene carbonate additive. The cell

was assembled in a glove box filled with dried argon gas (H_2O, $O_2 < 0.1$ ppm). All coin cells were standing for 3 days before electrochemical test.

GITT were performed on a Bio-Logic VMP3 multichannel electrochemical workstation. The charge/discharge measurements were carried out on a Neware measurement system at 25 °C. The charge/discharge profiles were attained at various current densities in the voltage range of 2.6–4.3 V. For GITT test, the cells were charged at 0.1 C for 30 min, followed by a relaxation of 10 h under open circuit. Na^+ diffusion coefficients were extracted by galvanostatic intermittent titration technique, according to the following equation:

$$D_{Na} = \frac{4}{\tau\pi}\left(\frac{m_B V_m}{M_B S}\right)^2\left(\frac{\Delta E_s}{\Delta E_\tau}\right)^2$$

Here, τ is the time of galvanostatic injection step, m_B is the weight of active material, V_m is the molar volume, M_B is the molar weight, ΔE_s is the value change between the neighboring charge open circuit potential (OCP), and ΔE_τ is the potential change during the galvanostatic injection step.

Characterization Methods

***In-situ* DEMS**: The gases generation during cell cycling were analyzed by *in-situ* differential electrochemical mass spectrometry (i-DEMS 100. Linglu Instruments. Shanghai). The parameter are as follows: Ion source is EI, 70 ev; Cell type is SWAGELOK configuration; Carrier gas is Argon with a speed of 0.7 mL/min; Detector is Secondary Electronic Multiplier with 1100 v. Monitor model chooses Selected Ion Monitor. The SWAGELOK cell configuration was assembled then relaxed for 6 h with Ar gas flowed. The loading mass of cathode is about 5 mg and the electrolyte is 150 uL. After 6 h relaxation, the SWAGELOK cell was charged to 4.3 V with a current density of 10 $\mu A\,mg^{-1}$.

SEM: SEM images were obtained on JEOL JSM-6390 microscope (Japan).

TEM: TEM images were acquired by a Hitachi HT-7700 transmission electron microscope (Japan) operating at 100 kV. High-resolution TEM (HRTEM) micrographs were obtained with a Philips Tecnai F20 FEG-TEM (The USA) operated at 200 kV. Samples for TEM analysis were prepared by drying a drop of cyclohexane solution containing the materials on the surface of a carbon-coated copper grid.

XPS: X-ray photoelectron spectra were conducted using a PHI 3 Quantera SXM instrument equipped with an Al X-ray excitation source (1486.6 eV). Binding energies (BEs) are referenced to the C1s of carbon contaminants at 284.8 eV. For XPS measurements, coin cells were prepared and charged/discharged to the target potential, then these cells were disassembled in argon-filled glovebox to avoid the contact with air. All electrodes were taken out from coin cells and washed with dimethyl carbonate (DMC) for three times. After standing for 1 h in vacuum, all electrodes were transfer to the instrument directly for subsequent test.

XRD: The X-ray diffraction XRD patterns were obtained using a Rigaku D/MAX-RB (Japan) with monochromatized Cu Kα radiation (λ=1.5418 Å) in the 2θ ranging from 10° to 70°. For *ex-situ* XRD measurements, coin cells were prepared and charged/discharged to the target potential, then these cells were disassembled in argon-filled glovebox. All electrodes were taken out from coin cells and washed with dimethyl carbonate (DMC) for three times. After standing for 2 h, all electrodes were sealed by Kapton tape for *ex-situ* XRD test. All powder patterns were refined using the Rietveld method as implemented in the GSAS[1] program. The crystal structure were visualized

by VESTA[2] and 3ds Max software.

First-principle calculations: In this work, we utilized Vienna Ab initio Simulation Package (VASP)[3-6] to perform DFT within periodic models. Generalized gradient approximation (GGA)[7] with projector augmented wave (PAW)[8, 9] method was applied in calculations to better simulate the electronic structures and the core-electron interaction. The cutoff energy is set to be 500 eV, and the force threshold of optimization convergence is 0.05 eV Å^{-1}. Here we employed Hubbard U potential to describe the Coulomb electron interaction precisely. Following previous literatures, we use the U values of Mn, Ni and Fe of 5 eV, 6 eV and 6 eV, respectively;[10] and J values of the three transition metal are set to be 1 eV. Structural optimizations were performed until the residual forces on each ion converged to smaller than 0.05 eV Å^{-1}. According to the experimental lattice of $Na_{0.66}Ni_{0.33}Mn_{0.66}O_2$, we built a (001) surface model with 2×2 supercell, and the vacuum layer has lengths more than 12 Å to avoid spurious interaction. The model of $Na_{0.33}Ni_{0.33}Mn_{0.66}O_2$ was built by removing half of the Na atoms in the slab. The Brillouin zone were meshed using $4 \times 4 \times 2$ Monkhorst-Pack grid[11] for all of the structural relaxations and electron localization function (ELF) calculations. For dense layer structure, we chose $2 \times 2 \times 2$. The energy change (ΔE) of introduction of a Na atom into the system is calculated as:

$$\Delta E = E_{\text{sys-Na}} - E_{\text{sys}} - E_{\text{Na}}$$

Where $E_{\text{sys-Na}}$ means the energy of the system containing Na, E_{sys} means the energy of the system, and E_{Na} indicate the energy of a Na atom, which is calculated from the Na primitive cell.

Figures and Tables
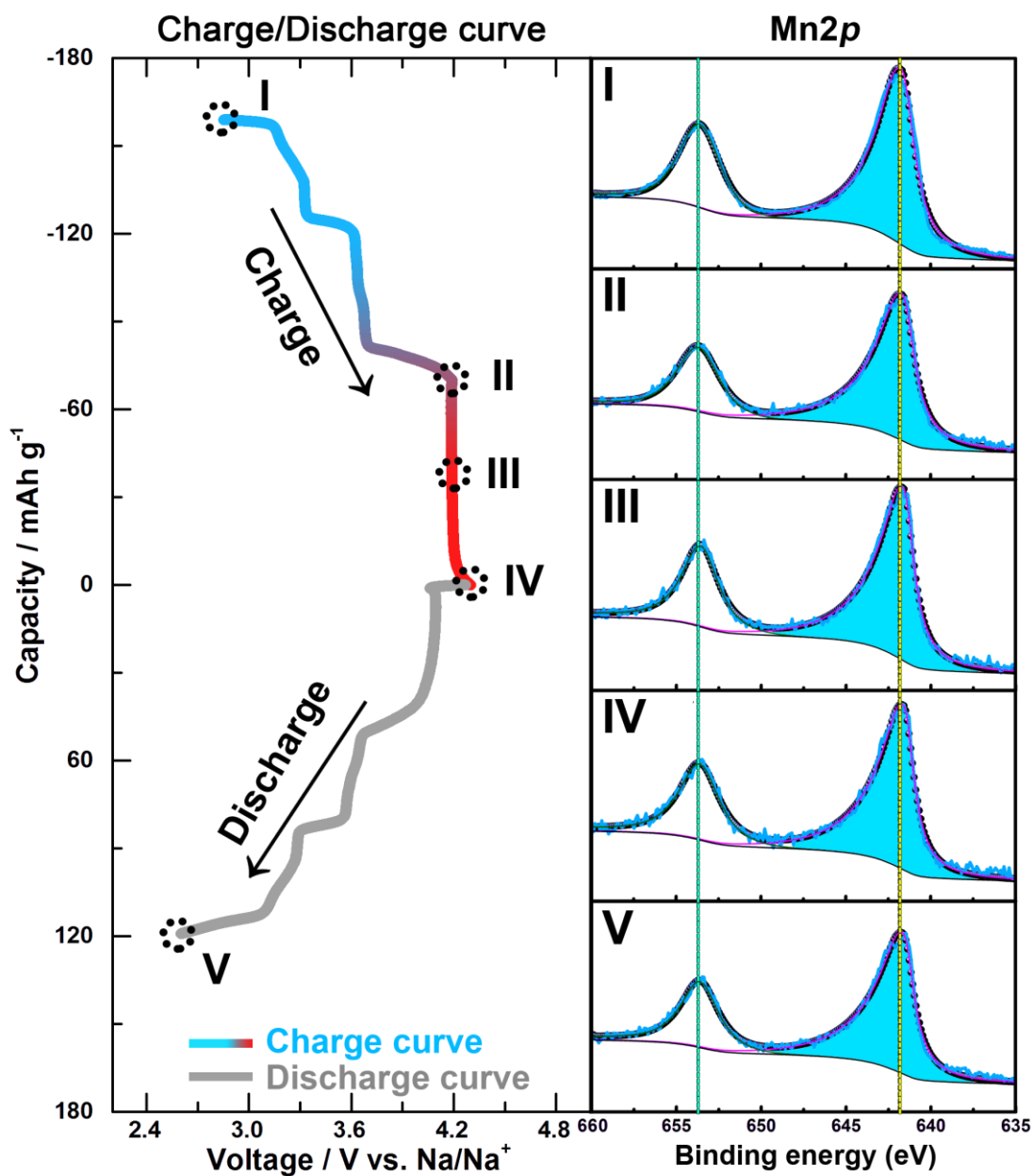
Figure S1. XPS analysis of Mn 2p core spectra at various charge state in Na$_{2/3}$Ni$_{1/3}$Mn$_{2/3}$O$_2$. The peaks remain unchanged during the whole charge/discharge process, hence Mn is not involved in the electrochemical reaction.
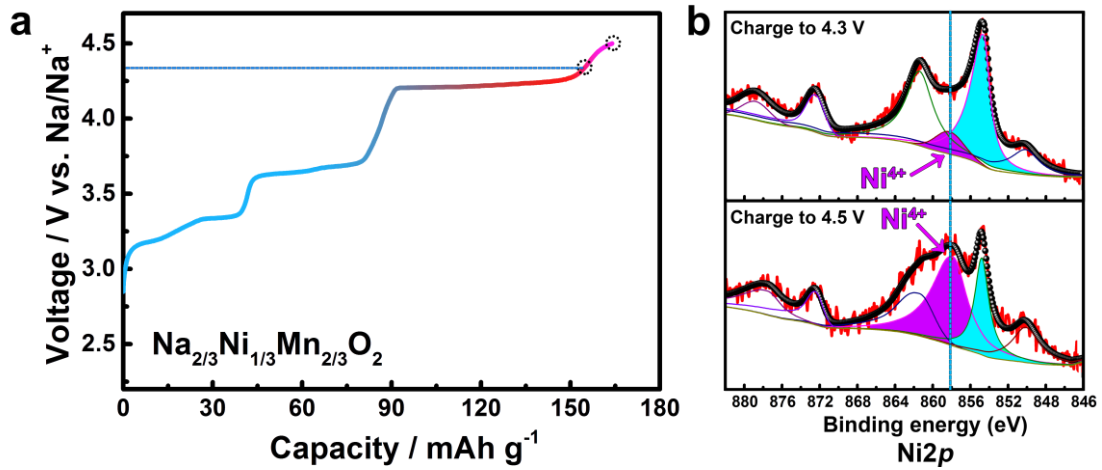
Figure S2. (a) Initial charge curve of $Na_{2/3}Ni_{1/3}Mn_{2/3}O_2$ with 4.5 V cut-off voltage. (b) XPS analysis of Ni $2p$ core spectra at 4.3V and 4.5V in $Na_{2/3}Ni_{1/3}Mn_{2/3}O_2$. The Ni^{4+} peak grow stronger when charge to 4.5 V, indicating that the main voltage region for $Ni^{3+} \rightarrow Ni^{4+}$ is above 4.3 V.
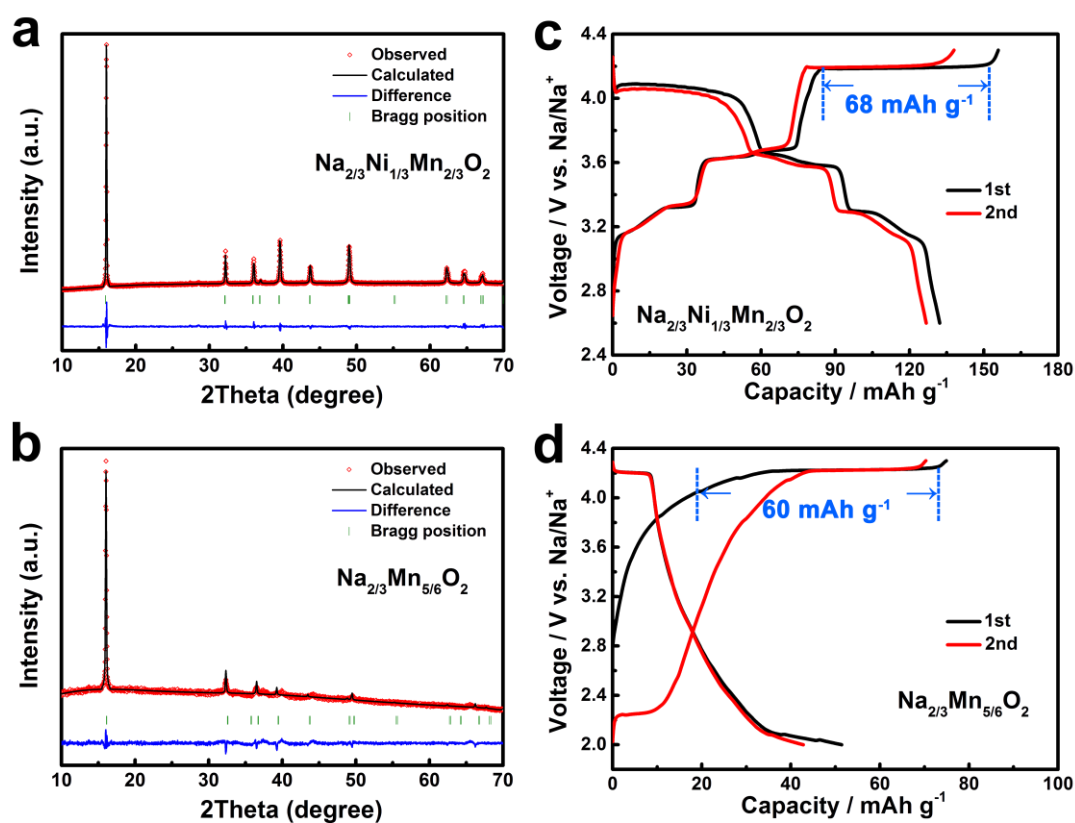
**Figure S3.** (a, b) The XRD and Rietveld plots of $Na_{2/3}Ni_{1/3}Mn_{2/3}O_2$ and $Na_{2/3}Mn_{5/6}O_2$. The refined crystallographic data were listed in Tables S1. (c, d) the charge/discharge curves of $Na_{2/3}Ni_{1/3}Mn_{2/3}O_2$ and $Na_{2/3}Mn_{5/6}O_2$ electrodes. When Ni^{2+} in $Na_{2/3}Ni_{1/3}Mn_{2/3}O_2$ is replaced by Mn^{4+}, the synthesized $Na_{2/3}Mn_{5/6}O_2$ can maintain the original P2 structure. Without Ni element, the $Na_{2/3}Mn_{5/6}O_2$ electrode still shows a long plateau at 4.2 V with 60 mAh g^{-1} capacity, which is very similar to the 4.2 V long plateau in $Na_{2/3}Ni_{1/3}Mn_{2/3}O_2$. Therefore, we speculate that the 4.2 V long plateau in $Na_{2/3}Ni_{1/3}Mn_{2/3}O_2$ is mainly contributed by oxygen redox rather than Ni^{3+}/Ni^{4+}.
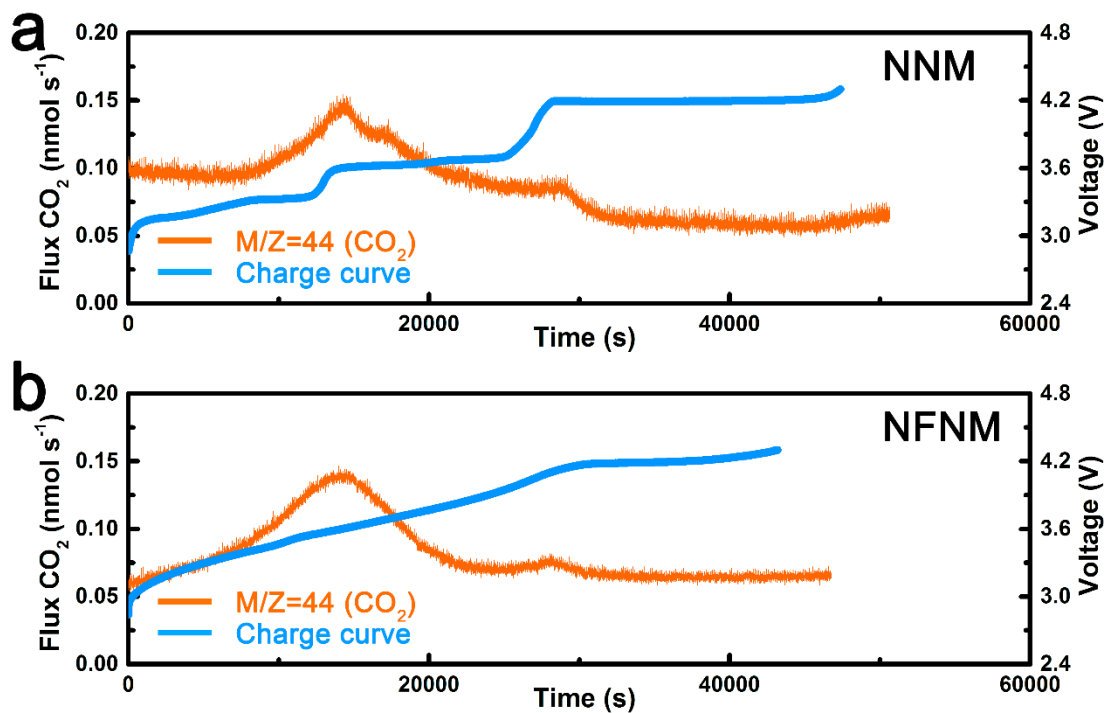
Figure S4. The release of CO_2 during the charge process for (a) NNM electrode and (b) NFNM electrode. Both NNM and NFNM electrodes show two CO_2 peaks around 3.6 V and 4.2 V.

We consider that the broad peak at 3.6 V is corresponded to the decomposition of PC electrolyte, The small peak around 4.2 V is corresponded to the decomposition of FEC additive. First of all, FEC decomposes into vinylene carbonate (VC) and fluoride ion, while the negatively charged fluoride ion reacts directly with sodium ions to form NaF. Then the VC further decomposes to release CO_2.
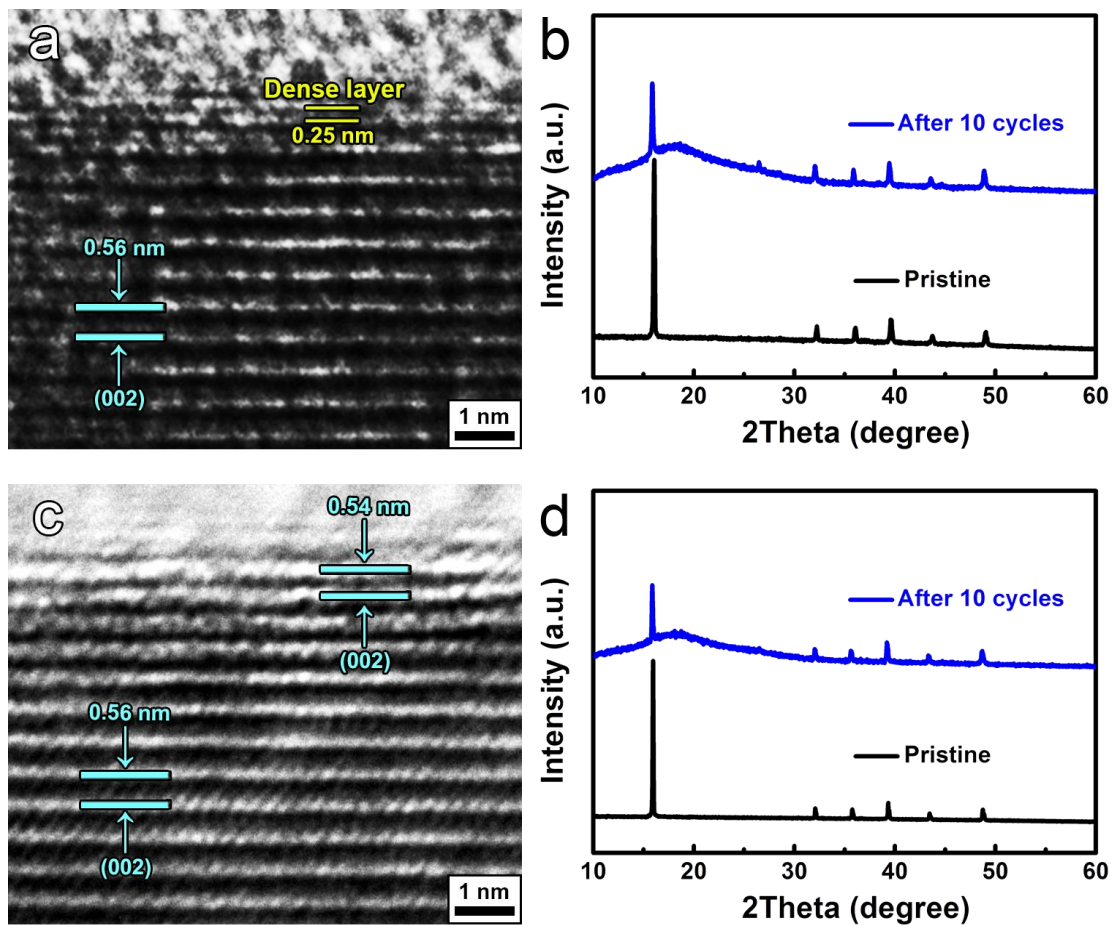
Figure S5. (a) HRTEM image of $Na_{2/3}Ni_{1/3}Mn_{2/3}O_2$ after 10 cycles. The interlayer distance of the surface structure is reduced to 0.25 nm, forming an inactive dense layer. (b) The XRD data of $Na_{2/3}Ni_{1/3}Mn_{2/3}O_2$ electrode after 10 cycles. (c) HRTEM image of $Na_{2/3}Fe_{2/9}Ni_{2/9}Mn_{5/9}O_2$ after 10 cycles. The surface structure still maintain P2 phase with almost no change in the interlayer distance. (d) The XRD data of $Na_{2/3}Fe_{2/9}Ni_{2/9}Mn_{5/9}O_2$ electrode after 10 cycles.
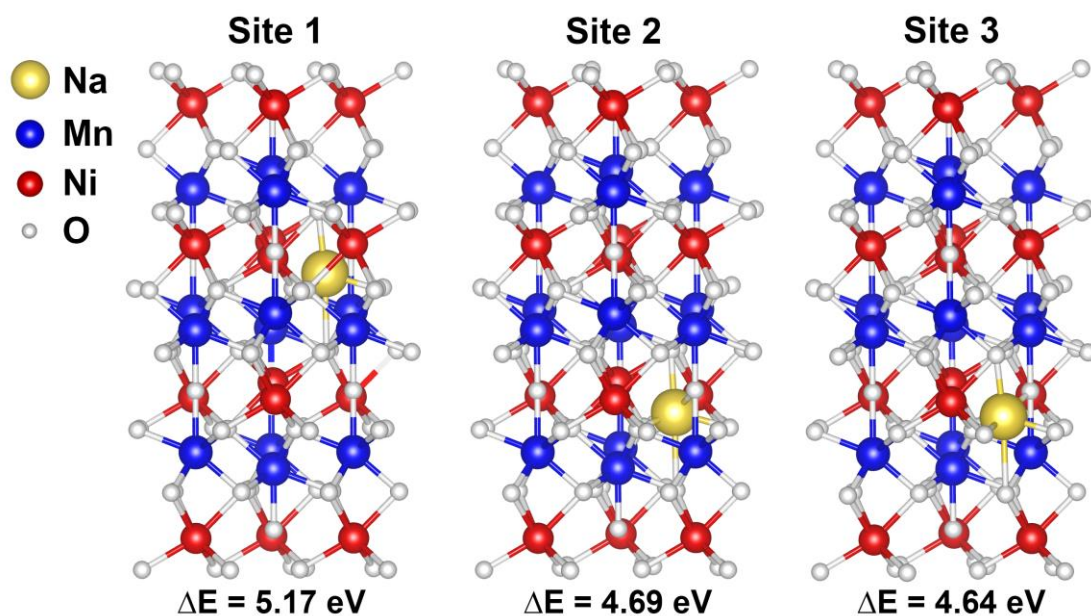
Figure S6. The varation of ΔE after the intercalation of Na^+ into the dense surface ($Ni_2Mn_2O_7$), which is calculated from the following equation: $\Delta E = E_{sys+Na} - E_{sys} - E_{Na}$. Where ΔE is the energy of the $Ni_2Mn_2O_7$ system in which a Na atom is embedded, E_{sys} means the energy of the $Ni_2Mn_2O_7$ system and E_{Na} denotes the energy of a Na atom calculated from Na primitive cell. When Na^+ intercalated into $Ni_2Mn_2O_7$ at site1 or site2 or site3, all ΔE show a huge increase, indicating that the dense is not suitable for Na^+ intercalation process. Therefore, the formation of the dense surface is the main reason for the large irreversible loss at initial cycle.
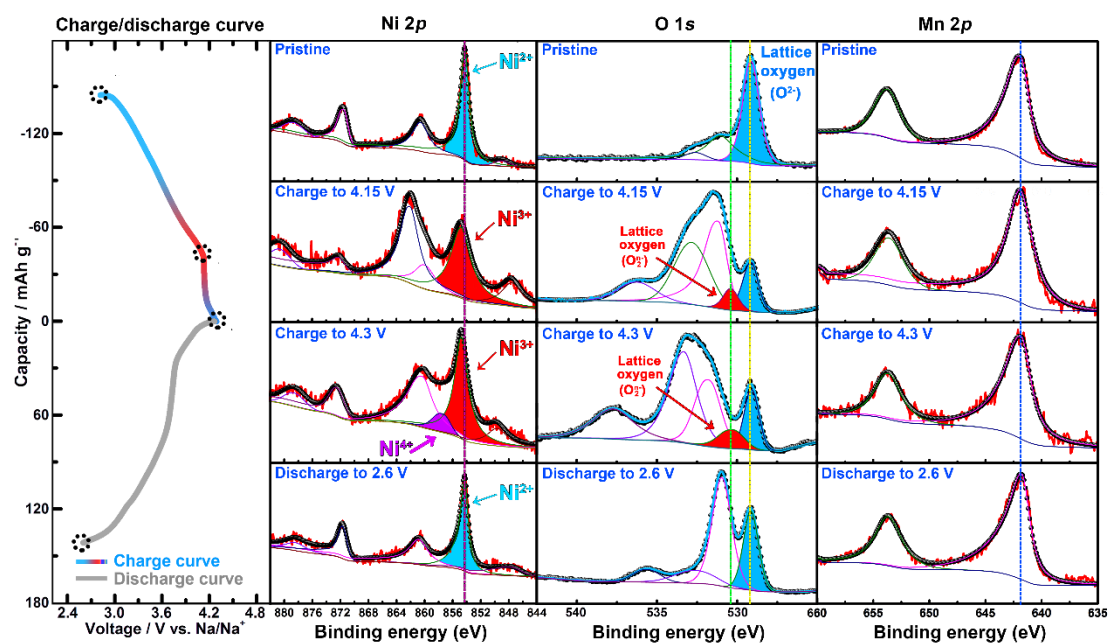
Figure S7. XPS analysis of Ni 2*p*, O 1*s* and Mn 2*p* core spectra at various charge state in $Na_{2/3}Fe_{2/9}Ni_{2/9}Mn_{5/9}O_2$. The peaks of Mn2*p* remain unchanged during the whole charge/discharge process, hence Mn is not involved in the electrochemical reaction. When charge to 4.15 V, Ni^{2+} is oxidized to Ni^{3+}. When charge to 4.3 V, Ni^{4+} starts to appear at 858.1 eV. When discharge to 2.6 V, the valence of Ni reduces to bivalence.

12
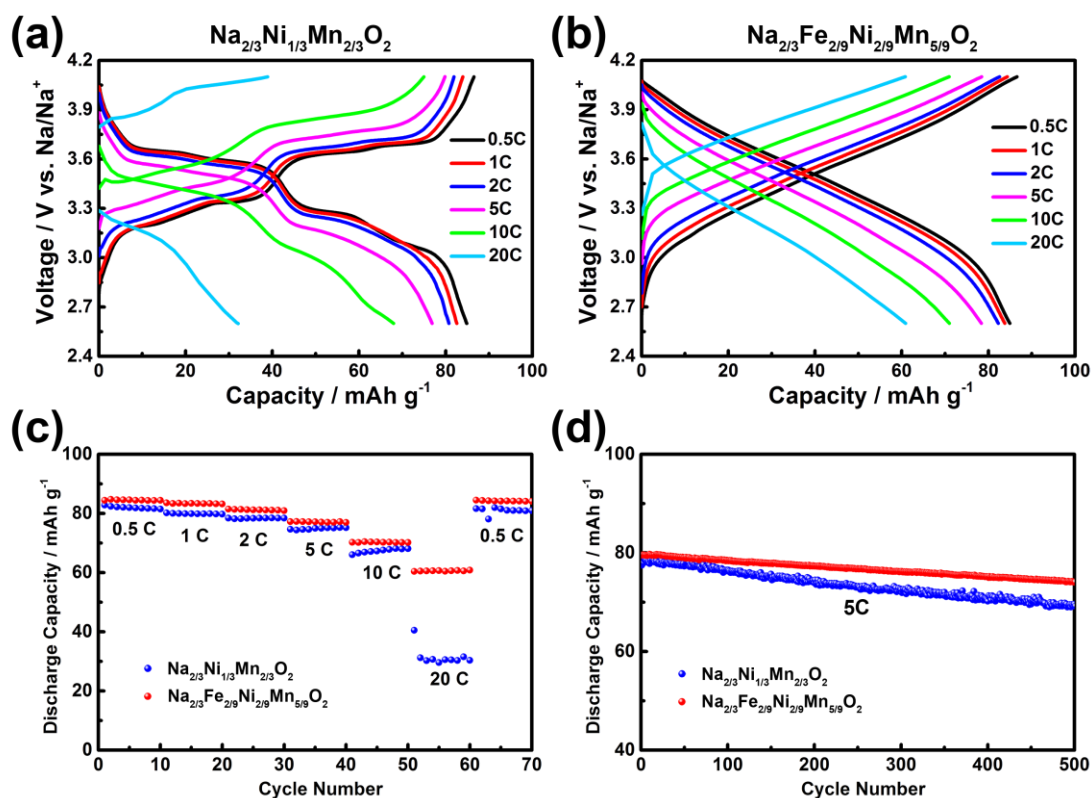
Figure S8. The electrochemical performance of $Na_{2/3}Ni_{1/3}Mn_{2/3}O_2$ and $Na_{2/3}Fe_{2/9}Ni_{2/9}Mn_{5/9}O_2$ in the voltage range from $2.6 \leq V \leq 4.1$ (the Na^+ removal range is $0 \leq z \leq 1/3$). The charge/discharge curves of $Na_{2/3}Ni_{1/3}Mn_{2/3}O_2$ obviously show two plateaus (Figure S9a), indicating the existence of two different Na^+ vacancy ordering arrangements.[12-15] This ordering arrangement usually induces higher Na migration energy barrier, leading to the poor Na kinetics.[12, 16, 17] These two voltage plateaus become smooth slope in $Na_{2/3}Fe_{2/9}Ni_{2/9}Mn_{5/9}O_2$, demonstrating the suppression of Na^+ vacancy ordering after substitution of Fe (Figure S9b). Therefore, the $Na_{2/3}Fe_{2/9}Ni_{2/9}Mn_{5/9}O_2$ electrode has higher Na^+ mobility than $Na_{2/3}Ni_{1/3}Mn_{2/3}O_2$ electrode. At high current density of 20 C (Figure S9c), the $Na_{2/3}Fe_{2/9}Ni_{2/9}Mn_{5/9}O_2$ electrode can deliver 60.4 mAh g^{-1} (71.5% retention) while $Na_{2/3}Ni_{1/3}Mn_{2/3}O_2$ shows lower capacity of 31 mAh g^{-1} (37.4% retention). As shown in Figure S9d, $Na_{2/3}Fe_{2/9}Ni_{2/9}Mn_{5/9}O_2$ shows higher capacity retention (94.2%) than that of $Na_{2/3}Ni_{1/3}Mn_{2/3}O_2$ (89.1%) after 500 cycles at 5 C.
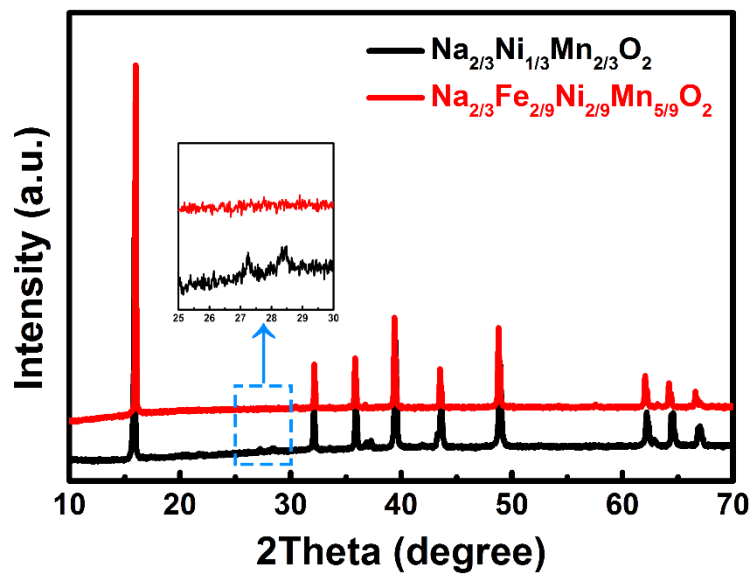
Figure S9. The comparison of the XRD patterns for NNM and NFNM samples. The superlattice peaks at 27.3° and 28.5° vanished after the substitution of Fe, indicating that Fe substitution can suppress the Na^+ vacancy ordering in Na layer.

Table S1. Crystallographic parameters of $Na_{2/3}Ni_{1/3}Mn_{2/3}O_2$, $Na_{2/3}Mn_{5/6}O_2$ and $Na_{2/3}Fe_{2/9}Ni_{2/9}Mn_{5/9}O_2$ refined by the Rietveld method.

Refine Result	a	b	c	V	R_p	R_{wp}
$Na_{2/3}Ni_{1/3}Mn_{2/3}O_2$	2.887078 Å	2.887078Å	11.155061 Å	80.523 Å^3	4.04%	5.69%
$Na_{2/3}Mn_{5/6}O_2$	2.898451 Å	2.898451 Å	10.992742 Å	79.978 Å^3	3.35%	4.95%
$Na_{2/3}Fe_{2/9}Ni_{2/9}Mn_{5/9}O_2$	2.903665 Å	2.903665 Å	11.178619 Å	81.623 Å^3	3.42%	5.62%

References

1. B. H. Toby, *J. Appl. Crystallogr.*, 2001, **34**, 210-213.
2. K. Momma and F. Izumi, *J. Appl. Crystallogr.*, 2008, **41**, 653-658.
3. G. Kresse and J. Hafner, *Phys. Rev. B*, 1994, **49**, 14251-14269.
4. G. Kresse and J. Hafner, *Phys. Rev. B*, 1993, **47**, 558-561.
5. G. Kresse and J. Furthmüller, *Comp. Mater. Sci.*, 1996, **6**, 15-50.
6. G. Kresse and J. Furthmüller, *Phys. Rev. B*, 1996, **54**, 11169-11186.
7. J. P. Perdew, K. Burke and M. Ernzerhof, *Phys. Rev. Lett.*, 1996, **77**, 3865-3868.
8. G. Kresse and D. Joubert, *Phys. Rev. B*, 1999, **59**, 1758-1775.
9. P. E. Blöchl, *Phys. Rev. B*, 1994, **50**, 17953-17979.
10. L. Li, L. Zhu, L.-H. Xu, T.-M. Cheng, W. Wang, X. Li and Q.-T. Sui, *J. Mater. Chem. A*, 2014, **2**, 4251-4255.
11. H. J. Monkhorst and J. D. Pack, *Phys. Rev. B*, 1976, **13**, 5188-5192.
12. R. Berthelot, D. Carlier and C. Delmas, *Nat. Mater.*, 2011, **10**, 74-80.
13. P. F. Wang, H. R. Yao, X. Y. Liu, Y. X. Yin, J. N. Zhang, Y. Wen, X. Yu, L. Gu and Y. G. Guo, *Sci. Adv.*, 2018, **4**, eaar6018.
14. D. H. Lee, J. Xu and Y. S. Meng, *Phys. Chem. Chem. Phys.*, 2013, **15**, 3304-3312.
15. R. J. Clément, J. Xu, D. S. Middlemiss, J. Alvarado, C. Ma, Y. S. Meng and C. P. Grey, *J. Mater. Chem. A*, 2017, **5**, 4129-4143.
16. G. J. Shu and F. C. Chou, *Phys. Rev. B*, 2008, **78**, 052101.
17. A. J. Toumar, S. P. Ong, W. D. Richards, S. Dacek and G. Ceder, *Phys. Rev. Appl.*, 2015, **4**, 064002.